RSC Advances

PAPER

View Article Online
View Journal | View Issue

Cite this: *RSC Adv.*, 2017, **7**, 44474

The origin of Mo promotion during H_2 pretreatment on an Fe catalyst for Fischer–Tropsch synthesis†

Liping Li,[a] Caixia Hu,[b] Wen Liu,[a] Peng Fei,[a] Xiaojing Cui,*[c] Yongwang Li[bc] and Jian Xu[b]

Received 3rd July 2017
Accepted 11th September 2017

DOI: 10.1039/c7ra07338k

rsc.li/rsc-advances

It is of vital importance but remains a grand challenge to understand comprehensively the effect of promoter elements on the active sites. Here, we report the experimental evidence of the origin of the promotion of molybdenum (Mo) during H_2 pretreatment on iron (Fe) catalysts for Fischer–Tropsch synthesis (FTS). By combing *in situ* laser Raman spectroscopy, Mössbauer spectroscopy, electron microscopy and *in situ* infrared spectroscopy, the promotion is related to the dispersion of Mo on the Fe surface during H_2 pretreatment, which inhibits the agglomeration of Fe and favors the formation of small Fe nanoparticles (NPs). The Mo coverage showed a strong dependency on the pretreatment temperature and the Mo amount in the FeMo catalyst. The strong Fe–Mo interaction caused by the Mo coverage weakened the activation of CO molecules on active Fe sites, which primarily accounts for the decline in the intrinsic activity (TOF_{CO}) of active Fe sites.

1. Introduction

The Fischer–Tropsch synthesis (FTS) process, which converts syngas into clean fuels, has been considered as an important and practical strategy to cope with the fuel shortage.[1,2] Iron-based catalysts are commonly used as catalysts for the industrial Fischer–Tropsch synthesis process.[3,4] Several metal elements are usually applied as promoters in iron-based catalysts, and they could tune the catalyst activity and selectivity remarkably.[3,5–14] Much work has been done to understand the promotional effect of the added metal elements, which has been demonstrated to originate from the electronic modification and/or the morphological change of the catalytically active iron centers.[5–14]

The iron-based catalysts are subjected to a pretreatment process before use. As the metal promoters exist commonly in the form of oxides in the prepared iron-based catalyst systems, they may be reduced and undergo structure reconstruction during the pretreatment process. Therefore, it is of vital importance to elucidate the dynamical evolutions of the metal promoters during the pretreatment and FTS processes in order to understand comprehensively their promotional effect. *In situ* characterizations provide possibilities to clearly understand the dynamic changes in the chemistry of the metal promoters in the iron-based FTS catalysts. However, this remains grand challenge for most of the *in situ* characterizations including *in situ* HRTEM and XPS that are sensitive to the structure and valence of the catalysts are commonly performed under conditions that are far from the FTS working conditions (such as vacuum condition and low temperatures).[15,16] Adding to this difficulty, the amounts of the metal promoters are usually minor in the iron-based FTS catalysts, which are near or below the detection limits for most characterization methods.[3,5–14]

Molybdenum nitride[17] and carbide[17,18] were reported to show excellent hydrogenation/isomerization activity and moderate FTS activity. In addition, molybdenum is applied as a promoter in the iron-based catalysts for coal indirect liquefaction and the FTS process.[19–24] Particularly for the iron-based FTS catalysts, the promotion of Mo has been demonstrated to shift the product spectrum to light hydrocarbons and reduce the catalyst deactivation caused by coke.[19–24] Many efforts are being paid to comprehensively understand the origin of this Mo promotion,[19–26] particularly at H_2 pretreatment.[19,20,26] Besides, the changes in the covalent state and morphology of Mo promoter during H_2 pretreatment and their effects on the structure and chemisorption behaviors of Rh were studied on supported Rh/ZrO_2 and Rh/SiO_2 catalysts for CO hydrogenation.[27–29] Agglomeration of Mo during pretreatment in CO and syngas (H_2/CO = 0.67) has been demonstrated in our previous studies, which caused the sintering of iron carbides and a loss in the activity.[25] In the present work, by combing *in situ* laser Raman

[a]College of Chemistry and Environmental Engineering, Shanxi Datong University, Datong, Shanxi 037009, People's Republic of China

[b]Synfuels China Technology Co. Ltd., Leyuan South Street II, No. 1, Yanqi Economic Development Zone C#, Huairou District, Beijing, 101407, People's Republic of China

[c]State Key Laboratory of Coal Conversion, Institute of Coal Chemistry, Chinese Academy of Sciences, Taiyuan, 030001, People's Republic of China. E-mail: cuixj@sxicc.ac.cn

† Electronic supplementary information (ESI) available. See DOI: 10.1039/c7ra07338k

spectroscopy, Mössbauer spectroscopy, electron microscopy and *in situ* infrared spectroscopy, we show the promotion of Mo during pretreatment in H_2 and how it affects the Fischer–Tropsch synthesis over iron catalyst.

2. Experimental section

2.1 Catalyst preparation

Iron–molybdenum catalysts were prepared by the same co-precipitation method reported in ref. 25 with iron nitrate $Fe(NO_3)_3 \cdot 9H_2O$ and ammonium heptamolybdate $(NH_4)_6Mo_7O_{24} \cdot 4H_2O$. In brief, the iron nitrate solution was added into a solution of ammonium heptamolybdate (pH = 2). NH_4OH was then added dropwisely at 80 °C into the mixed solution until a pH of 6 was reached. The resulted iron and molybdenum precipitate was aged under vigorous stirring at 90 °C for 3 h, followed by filtering and drying at 120 °C for 48 h. The catalyst samples were then calcinated at 375 °C for 10 h. The unpromoted iron catalyst was obtained by precipitated nitrate of iron according to the method described above. The prepared catalysts were designated as 100Fe for the unpromoted iron catalyst, and $100Fe_2Mo$, $100Fe_5Mo$, $100Fe_8Mo$ and $100Fe_{10}Mo$ (the molar ratio of Fe/Mo = 100 : 2, 100 : 5, 100 : 8 and 100 : 10) respectively for the iron–molybdenum bimetallic catalyst precursors.

2.2 Catalyst characterization

The BET surface area, pore volume and pore size distribution of the catalyst precursors were determined *via* nitrogen physisorption at the normal boiling point of N_2 (−196 °C) using an ASAP 2420 (Micromeritics, USA).

Powder X-ray diffraction (XRD) measurements of the catalyst precursors were carried out using a D/max-RA X-ray diffratometer (Rigaku, Japan), equipped with Cu Kα radiation (λ = 1.5406 Å) at 40 kV and 150 mA. The patterns were scanned at a rate of 2° min^{-1} from $2\theta = 10°$ to 80°.

HRTEM characterization was performed at a JEOL 2010 HRTEM (JEOL, Japan) using an accelerating voltage of 200 kV. The samples were dispersed in ethanol and mounted on a carbon foil supported on a copper grid. TEM images and EDS mapping of Fe and Mo in calcined $100Fe_{10}Mo$ were obtained using a FEI Tecnai 20 TEM with an accelerating voltage of 200 kV.

H_2 temperature programmed desorption (H_2-TPD) characterization was performed in a quartz tube on an AutoChem II 2920 chemisorption analyzer. In each experiment, 100 mg of the sample was pretreated *in situ* in a flow of 5% H_2/95% Ar at 350 °C for 12 h (30 mL min^{-1}). After purging with a Ar flow of 30 mL min^{-1} for 0.5 h at 350 °C to exclude physisorbed H_2, the sample was cooled down to 50 °C and 10% H_2/90% Ar was purged into the quartz microreactor with a flow rate of 30 mL min^{-1} and kept for 0.5 h. Then, the sample was purged in Ar at 50 °C for 0.5 h, and heated from 50 °C to 850 °C at a rate of 10 °C min^{-1}. The desorbed H_2 was monitored by a thermal conductivity detector (TCD). The H_2-TPD profiles of $100Fe_5Mo$ and $100Fe_{10}Mo$ were fitted using a nonlinear least-squares method with a Gaussian function.

LRS spectra of catalyst precursors and *in situ* Laser Raman spectra (LRS) were obtained by a Horiba-Jobin Yvon LabRam HR Raman System using a UV-sensitive liquid N_2 cooled CCD detector (Horiba-Jobin Yvon CCD-3000V) and a UV laser (λ = 325 nm) as the ray source which was set to an output power of 30 mW. The laser was focused on the samples with a confocal microscope equipped with a 15× objective (OFR LMU-15X-NUV). An appropriate homemade stainless cell was designed with a double-walled quartz window at the top and an internal heating system. One set of stainless steel gas lines was connected to the cell, which allows *in situ* pretreatment. The catalyst samples which was pressed and sieved to 60–80 mesh was loaded in a stainless reactor and was then mounted in vertical position inside the cell. The catalyst sample was *in situ* pretreated in 5% H_2/95% Ar (by mole basis) at a rate of 10 °C min^{-1} to 350 °C and held for 200 min. The Raman spectra were taken at 350 °C.

The Mössbauer spectra (MES) at 20 K were collected using a CANBERRA series 40 MCA constant-acceleration drive with a triangular reference signal. The γ-ray source was a ^{57}Co in Pd matrix. The Mössbauer spectra were analyzed using a nonlinear least squares fitting procedure with a set of independent Lorentzian lines including singlets, quadruple doublets, and/or magnetic sextets.

In situ CO-Diffuse Reflectance Fourier Transform Infrared spectroscopy (CO-DRFTIR) spectra were recorded with a resolution of 4 cm^{-1} on an FT-IR spectrometer supplied with a detector and a diffuse reflectance attachment. A stainless cell was designed with two ZnSe windows at the top sphere and an internal heating system. It was connected with one set of stainless steel gas lines, allowing *in situ* pretreatment and CO chemisorption. About 30 mg catalyst was *in situ* pretreated in flowing 5% H_2/95% Ar or 5% CO/95% He at 280 or 350 °C for 12 h. For H_2 pretreatment, the sample was purged with Ar for 0.5 h and cooled down to 20 °C in Ar; for CO pretreatment, the sample was purged with He for 0.5 h and cooled down to 20 °C in He. A set of experiments was performed at 20 °C on the *in situ* pretreated samples by gradually pulsing different amounts (0.1–4 mmol) of CO and recording the spectra after each dosage. After CO adsorption on the sample reached saturation, the flowing He was passed through the sample until no adsorption of molecular CO was detected. The final spectrum at the end of He purging process was recorded.

2.3 Catalyst testing

2 g of the catalyst precursor was mixed with 20–40 mesh quartz granules up to 3 cm^3. The mixture was loaded into the isothermal section of a fixed-bed reactor. The catalyst pretreatment was carried out *in situ* with a stream of H_2 under 280 °C or 350 °C, 1 atm and 6 NL per g-cat per h for 12 h. The reactor was cooled down to 200 °C and then pressurized up to 1.5 MPa. The temperature was gradually increased to 280 °C. FTS reaction was carried out in a flow of syngas (H_2/CO = 1.6) at 280 °C and 3 NL per g-cat per h. Both the purified feed gases and the tail gas were analyzed by on-line gas chromatographs (GCs, models 6890N and 4890D; Agilent) and its flow rate was measured by a wet-gas flowmeter.

3. Results and discussion

As shown in Table S1 in ESI,† with the molar ratio of Mo/Fe in the catalyst increasing from 2/100 to 10/100, the BET surface area increased from 41 to 157 $m^2\ g^{-1}$ while the average pore size decreased from 5.5 to 3.3 nm. The average crystallite sizes of α-Fe_2O_3 in the FeMo catalyst precursors were calculated using Scherer's equation taking diffraction peak at $2\theta = 33°$.[30] As shown in Table S1 and Fig. S1 in ESI,† the particle size of α-Fe_2O_3 decreased continuously with the increase of Mo loading level. As indicated by XRD, the particle size of α-Fe_2O_3 in 100Fe was estimated to be 32 nm, which was decreased to 30, 17 and 14 nm in $100Fe_2Mo$, $100Fe_5Mo$ and $100Fe_8Mo$, respectively. $100Fe_{10}Mo$, however, can't be accurately estimated by the Scherer's equation since its diffraction peaks were poorly resolved. For further evaluation of size distributions of α-Fe_2O_3 in the FeMo catalyst precursors, HRTEM characterization were carried out, as shown in Table S1 and Fig. S2 in ESI.† The average particle sizes of α-Fe_2O_3 estimated by HRTEM decreased from 23 and 6 nm as a function of Mo loading level (from $100Fe_2Mo$ to $100Fe_{10}Mo$). Furthermore, the evolution of Mo in $100Fe_{10}Mo$ during the preparation process was investigated by LRS (Fig. S3 and Table S2 in ESI†). $Fe(NO_3)_3 \cdot 9H_2O$ and $(NH_4)_6MoO_{24} \cdot 4H_2O$ were also studied for the accurate assignment of LRS peaks. No bands of Mo were detected after precipitation. A band at 947 cm^{-1} appeared after drying. This band can be attributed to Mo=O vibration in $Mo_7O_{24}^{6-}$ compared with the result of $(NH_4)_6MoO_{24} \cdot 4H_2O$, in accordance with the literature.[31] After calcination, the bands of polymer Mo species and MoO_3 particles were observed. This result indicated the agglomeration of Mo (from highly dispersed state into polymerized/crystallite state) during the preparation. MoO_3 in the FeMo catalysts were, as indicated by HRTEM, nanoparticles with an average particle size smaller than 8 nm (Fig. S4 in ESI†). The uniform distribution of Mo in the catalyst precursor was verified by EDS analysis (Fig. S5 in ESI†).

The FTS performance of all the H_2 pretreated catalysts was tested in a fixed bed reactor. The CO conversion is used as a measurement of FTS reactivity (Table 1 and Fig. S6 in ESI†). No activity was observed on MoO_3 reduced under the same conditions with the FeMo catalysts. Therefore, the variety in the catalyst activities should result from the difference in the nature of active iron particles. The initial activity of 100Fe was nearly 50% (TOS = 24 h), which declined quickly and reached steady-state after TOS = 72 h (Fig. S6 in ESI†). For the FeMo catalysts, the induction period were about 24 to 48 h (Fig. S6 in ESI†). On the basis of this result, the activities of all the catalysts were compared at a TOS of 72 h. $100Fe_2Mo$ catalyst showed highest activity among all the catalysts and its activity was about thrice as high as that of 100Fe. The activity declined with the further increment in the Mo loading level. Although the activity of $100Fe_{10}Mo$ was lowest among all the FeMo catalysts, it was about twice as high as that of 100Fe. The enhancement effect of Mo on the activity was also obvious after reaction for 192 h. The strong interdependency can be observed between the product distribution of the FeMo catalysts and the amount of Mo. The selectivity to lighter hydrocarbons, *i.e.*, CH_4 and C_2–C_4, was increasingly promoted while that of C_5^+ hydrocarbons was depressed by the increment in the Mo amount (Table 1). Besides, the addition of Mo largely promoted the selectivity of CO_2, which was two or three times of that of 100Fe catalyst. The effect of Mo on promoting the light hydrocarbons and CO_2 has also been demonstrated.[19–26]

To understand the origin of the catalytic reactivity over FeMo catalysts, we further investigated the dynamic changes in the structure and morphology of Fe and Mo in the catalysts during pretreatment in H_2. The dynamic migration of Mo during the H_2 pretreatment was detailed by *in situ* LRS (Fig. 1). For better comparison, the LRS characterization of all the catalyst precursors was also performed. The band at *ca.* 323 cm^{-1} in the spectra of all the catalysts was caused by the laser (325 nm). The bands characteristic of hematite was observed in the spectrum of 100Fe catalyst precursor.[32] A small band at 990 cm^{-1} and a broad band in the 760–950 cm^{-1} region showed up in the spectra of the FeMo catalyst precursors, which are assigned to crystalline MoO_3 and a combination of the bands of hematite (803 cm^{-1}) with the surface molybdates (Mo–O–Mo functionalities).[33] The reduction of 100Fe in H_2 at 350 °C caused the

Table 1 The FTS performances of iron and iron–molybdenum catalysts[a]

	Particle size[b] (nm)			TOF[e]	Hydrocarbon selectivity, wt%					
Catalyst	XRD[c]	TEM[d]	CO conv.%	mol_{CO} per $mmol_{Fe}$ h	CH_4	C_2	C_3	C_4	C_5^+	CO_2 mol%
MoO_3	—	—	0	0	0	0	0	0	0	0
100Fe	36	29	33.6	1164.9	11.6	13.5	19.2	14.0	41.7	19.6
$100Fe_2Mo$	28	—	94.4	2306.6	21.3	15.2	19.2	11.6	32.7	44.9
$100Fe_5Mo$	20	14	75.8	852.8	23.3	17.3	20.3	13.0	26.1	36.6
$100Fe_8Mo$	19	—	80.6	537.6	24.9	19.6	21.6	12.4	21.5	45.0
$100Fe_{10}Mo$	13	10	68.4	475.6	31.4	17.5	19.2	10.9	21.0	45.0

[a] Reaction condition: 280 °C, $H_2/CO = 1.6$, GHSV = 3 NL per g-cat per h, TOS = 72 h. [b] The catalysts after pretreatment in H_2 at 350 °C for 12 h. [c] The average size of α-Fe in the pretreated catalysts was calculated using Scherer's equation taking the diffraction peak at $2\theta = 42.9°$. [d] The average iron crystallite size of the pretreated catalysts was calculated from HRTEM data. [e] TOF = mmol converted $_{CO}$/($mmol_{Fe}$ h), where $mmol_{Fe}$ represents the mole of the total surface Fe atoms in each catalyst which are obtained based on XRD result, the mol_{Fe} values of the catalysts are calculated and listed in Table S5 in ESI.

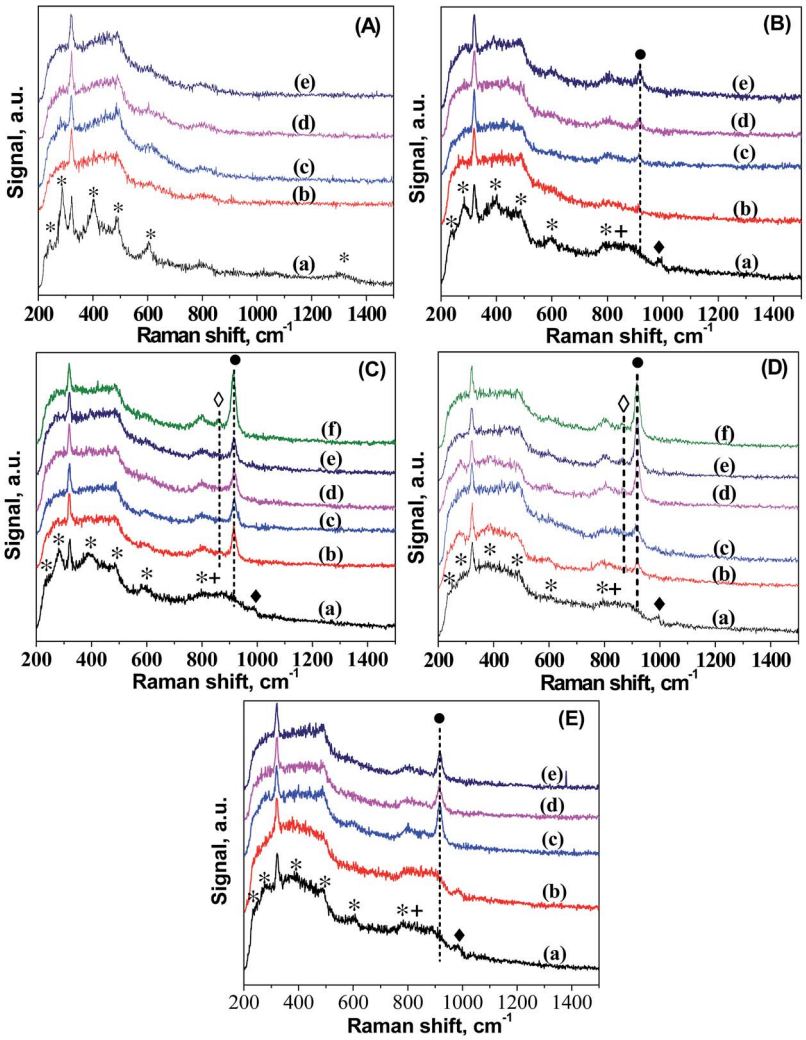

Fig. 1 *In situ* LRS results of: (A) 100Fe after calcination (a), and reduced in H_2 at 350 °C for (b) 120 min, (c) 175 min, (d) 180 min, (e) 200 min; (B) $100Fe_5Mo$ after calcination (a), and reduced in H_2 at 350 °C for (b) 55 min, (c) 72 min, (d) 98 min, (e) 188 min; (C) $100Fe_8Mo$ after calcination (a), and reduced in H_2 at 350 °C for (b) 102 min, (c) 182 min, (d) 193 min, (e) 204 min (f) 219 min; (D) $100Fe_{10}Mo$ after calcination (a), and reduced in H_2 at 350 °C for (b) 55 min, (c) 65 min, (d) 100 min, (e) 130 min, (f) 195 min; (E) $100Fe_{10}Mo$ after calcination (a), and reduced in H_2 at 280 °C for (b) 85 min, (c) 182 min, (d) 204 min, (e) 217 min.

gradual disappearance of some hematite bands, indicating the reduction of hematite. For FeMo catalysts, the band of MoO_3 diminished, followed by the formation of a new band at 918 cm^{-1} that can be assigned to symmetric stretching mode of Mo=O bond in tetrahedral surface molybdates (isolated).[34–37] This result indicated the dispersion of crystalline MoO_3 in the FeMo catalysts during reduction in H_2, forming isolated molybdate species. This Mo dispersion was more obvious at higher Mo loading levels, as indicated by the higher band intensity of isolated molybdate species. For $100Fe_8Mo$ and $100Fe_{10}Mo$ catalysts, a band at 864 cm^{-1} appeared as the reduction time prolonged, which was attributed to the asymmetric stretching of Mo–O–Mo bond in octahedral surface molybdates (polymerized).[34,35,38–40] It seems that the enrichment in the surface isolated molybdates caused the formation of polymerized molybdates. Besides, the pretreatment at high temperatures accelerated the spreading of Mo in the FeMo catalysts (Fig. 1D and E).

The spreading of MoO_3 on oxide supports has been studied by *in situ* LRS.[34] It was interpreted as a solid–solid wetting process driven by the surface free energy reduction, *i.e.*, "carpet unrolling" mechanism, and its spreading rate was found to be accelerated by the water vapor.[41] To explain this, the spreading process was suggested to following eqn (1) and (2), that is crystalline MoO_3 interacted with water to form the mobile species-oxyhydroxide $(MoO_2(OH)_2)$[42,43] which interacted with

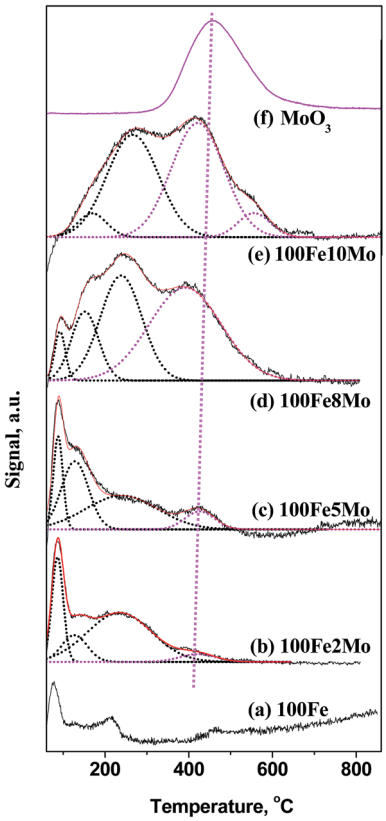

Fig. 2 H_2-TPD profiles of iron and iron–molybdenum catalysts.

surface hydroxyls to form isolated surface molybdates (MoO_4^{2-}).[43,44] A further increase in the surface concentration of these isolated molybdates would lead to the formation of polymerized molybdates. This explanation correlated well with our *in situ* LRS observations. This is reasonable since a large amount of water vapor would form during reduction of the FeMo catalyst precursor in H_2, particularly at high temperatures. The formed water vapor would facilitate the spreading of MoO_3 on the surface of the iron species.

$$MoO_3 + H_2O \rightarrow MoO_2(OH)_2 \quad (1)$$

$$MoO_3 + 2OH^- \rightarrow MoO_4^{2-} + 2H_2O \quad (2)$$

Once the pretreatment started, the band intensities of mono- and poly-molybdates developed rapidly to high levels particularly for $100Fe_8Mo$ and $100Fe_{10}Mo$ catalysts. Note that the increment in the intensities of these two bands is much larger than the decrement in that of MoO_3 in the FeMo catalysts. It is therefore possible that the enrichment of Mo species from the bulk to the surface of the catalysts occurred during the reduction, resulting in a catalyst surface richer in Mo species.

H_2-TPD experiments were carried out to verify further the Mo coverage on the Fe surface during H_2 pretreatment (Fig. 2). For 100Fe catalyst, the two desorption peaks appeared at about 75 and 210 °C, which can be attributed to the adsorbed hydrogen on metallic iron and reduced iron oxides respectively.[45,46] The high-temperature desorption peaks (>300 °C) that was absent on the profile of 100Fe, appeared at the profiles of the FeMo catalysts. Therefore, the high-temperature desorption peaks likely attributed to the hydrogen species that adsorbed on the reduced Mo surface. To verify this assumption, the H_2-TPD profile of MoO_3 was also performed. As expected, all the desorption peaks for pure Mo surface (MoO_3) showed up at a temperature range of 300–600 °C, in good accordance with the literature.[47] The large difference in the chemisorption temperatures of hydrogen on the reduced surface Mo and Fe sites facilitates the distinction of surface Mo from surface Fe in the FeMo catalysts.

Based on the literature[45–47] and our H_2-TPD analysis, the desorption peaks below 300 °C were assigned to the hydrogen species on the surface Fe sites, while those above 300 °C were originated from the hydrogen species on the surface Mo sites. Notably, the H_2 chemisorbed on the surface Mo sites appeared in $100Fe_2Mo$ and became dominant in $100Fe_{10}Mo$. This result implied that the coverage effect of Mo was largely promoted with the increase in the Mo loading levels, consistent with the *in situ* LRS result. The H_2-TPD profiles of the FeMo catalysts were further fitted to acquire the relative amount of surface Fe and Mo sites and the coverage ration of Mo (θ_{Mo}) (Table S3 in ESI†). The θ_{Mo} for $100Fe_2Mo$ and $100Fe_5Mo$ were below 10%, which increased to round 50% for $100Fe_8Mo$ and $100Fe_{10}Mo$. The unexpected high coverage of Mo on the Fe surface correlated well with the *in situ* LRS results, *i.e.*, the migration of Mo from the bulk to the surface of the FeMo catalysts.

The effect of Mo dispersion on the morphology and electronic properties of active iron particles were further investigated. Much smaller α-Fe particles were formed in FeMo catalysts than 100Fe catalyst, as indicated by HRTEM (Fig. S7 in ESI†) and XRD (Fig. S8 in ESI†). The average size of α-Fe estimated by XRD and HRTEM declined with the enhancement in the Mo loading level (Table 1). As indicated by *in situ* LRS results, the spreading of Mo during the pretreatment occurred. The Mo dispersion enhanced the segregation effect of Mo on the iron particles, which inhibited effectively the agglomeration of Fe and favored the formation of small Fe particles. MES was performed at 20 K to accurately identify the distributions of iron

Table 2 Mössbauer parameters at 20 K of Fe and FeMo catalysts after H_2 pretreatment and after FTS reaction

		Area (%)			
Procedure	Phases	100Fe	$100Fe_5Mo$	$100Fe_8Mo$	$100Fe_{10}Mo$
H_2, 280 °C[a]	α-Fe	67.3	2.7	1.1	24.8
Reduced	Fe_3O_4	32.7	97.3	98.9	75.2
H_2, 350 °C[b]	α-Fe	100.0	59.8	26.7	34.1
Reduced	Fe_3O_4	—	40.2	73.3	65.9
H_2, 280 °C[c]	ε-$Fe_{2.2}C$	14.3[e]	22.3	10.5	37.2
Used	Fe_3O_4	85.7	77.7	89.5	62.8
H_2, 350 °C[d]	ε-$Fe_{2.2}C$	16.8[e]	31.9	65.4	57.9
Used	Fe_3O_4	83.2	68.1	34.6	42.1

[a] Pretreated in H_2 at 280 °C for 12 h. [b] Pretreated in H_2 at 350 °C for 12 h. [c] Pretreated in H_2 at 280 °C for 12 h, followed by FTS reaction for 72 h. [d] Pretreated in H_2 at 350 °C for 12 h, followed by FTS reaction for 72 h. [e] The iron carbide for the used 100Fe catalyst was χ-Fe_5C_2.

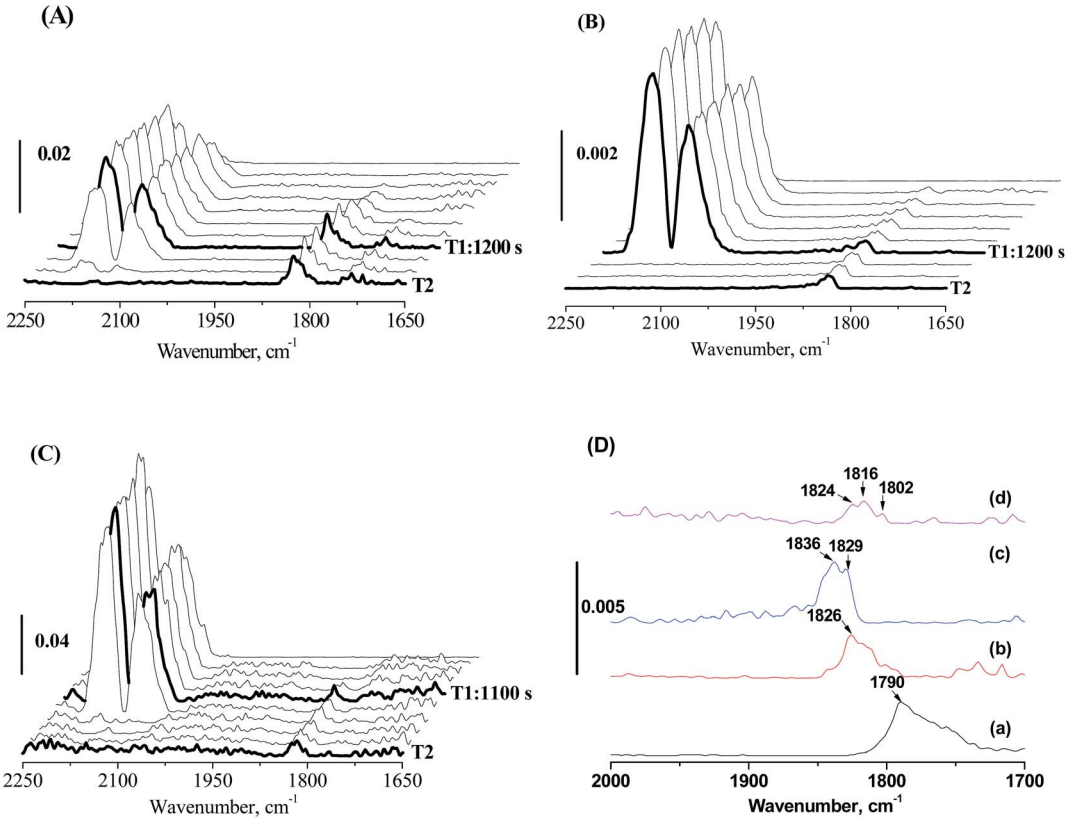

Fig. 3 *In situ* CO-FTIR profiles of $100Fe_{10}Mo$ pretreated in 5% H_2/95% Ar for 12 h at (A) 280 °C and (B) 350 °C, (C) pretreated in 5% CO/95% He for 12 h at 350 °C and (D) the profiles at 1700–2000 cm^{-1} region at T2: (a) 100Fe pretreated in H_2 at 350 °C, $100Fe_{10}Mo$ pretreated in H_2 at (b) 280 °C and (c) 350 °C, and (d) $100Fe_{10}Mo$ pretreated in CO at 350 °C. T1, when CO adsorption was saturated; T2, when molecule CO adsorption was completely removed.

phases in the pretreated and used catalysts (Tables 2, S4 and Fig. S9–S12 in ESI†). Notably, after pretreatment at 350 °C in H_2, the α-Fe content of $100Fe_8Mo$ and $100Fe_{10}Mo$ catalysts were lower than that of $100Fe_5Mo$ catalyst. Although several experimental observations have shown the inhibition effect of Mo on the reduction of iron FTS catalyst,[19–26] the origin of this phenomenon are not comprehensively understood. The Mo dispersion occurred during pretreatment inevitably caused the coverage of Mo on the catalyst surface. As the Mo dispersion was boosted by the rise of the Mo loading level, the coverage effect of Mo would be more severe at high Mo loading levels. This coverage effect of Mo hindered the reduction of Fe_2O_3 to α-Fe. During the FTS reaction, α-Fe phase in the FeMo catalysts transformed into ε′-$Fe_{2.2}C$ while χ-Fe_5C_2 was formed in 100Fe. The amount of χ-Fe_5C_2 in the used 100Fe was much lower than that of α-Fe in the reduced 100Fe. In contrast, the amount of ε′-$Fe_{2.2}C$ in the used FeMo catalysts maintained. This result implied the superior stability of iron carbides in the FeMo catalysts, which is likely resulted from the coverage effect of Mo.

As a first approximation, one can assume that the active Fe crystallites in pretreated 100Fe and FeMo catalysts possess a particle size identical to the average size estimated by XRD (Table 1 and Fig. S8 in ESI†). Furthermore, the active Fe sites in FeMo catalysts own the Mo coverage (θ_{Mo}) estimated by H_2-TPD (Table S3 in ESI†). Given this assumption, we estimate the total amounts of the pure surface iron species in all the catalysts (Table S5 in ESI†) and the corresponding intrinsic activity for CO (TOF_{CO}). As listed in Table 1, TOF_{CO} was promoted at low amount of Mo ($100Fe_2Mo$) and largely declined with the increment in the Mo amount. Particularly for $100Fe_5Mo$, $100Fe_8Mo$ and $100Fe_{10}Mo$, although the addition of Mo promoted the overall activity, it caused a loss in TOF_{CO}. This result implied the detrimental effect of Mo on the intrinsic activity of Fe at high Mo amount.

This decline in the intrinsic activity at high Mo loading levels indicated the strong modification of Mo on the electronic properties of active Fe sites. The strong modification of Mo likely originates from pretreatment-induced coverage effect of Mo. With MoO_x species/layers covering part of the Fe nanoparticles, the interaction of Fe with Mo becomes strong. To prove this assumption, *in situ* CO-FTIR experiments was performed to explore the chemisorption behaviors of CO on 100Fe and $100Fe_{10}Mo$ catalyst (Fig. 3). This is based on the understanding that the adsorption of reactants on the active Fe sites that were strongly interacted with Mo would be different from those with weak and no Fe–Mo interactions. $100Fe_{10}Mo$ catalyst was chosen as a representative of the FeMo catalysts. The Fe–Mo interaction can be tuned simply by regulating the pretreatment protocols. As indicated by the *in situ* LRS, for H_2 pretreatment, the Fe–Mo interaction can be tuned by regulating the

pretreatment temperature, and a stronger Fe–Mo interaction can be achieved at 350 °C than at 280 °C. Besides, the agglomeration of Mo and the consequent phase separation of Fe and Mo was identified during CO pretreatment.[25] In such conditions the Fe–Mo interaction would be largely weakened.

No CO adsorption bands were observed in the *in situ* CO-FTIR spectra of MoO_3, indicating that CO only adsorbed on the iron sites. The bands at about 1790 cm^{-1} on 100Fe can be attributed to the multiply bridge-bonded CO on deep hollow Fe sites,[48,49] while these bands were shifted largely towards the higher wavenumber direction to 1843–1816 cm^{-1} for $100Fe_{10}Mo$ catalysts (Fig. 3D). The frequencies of these bands located at about 1826 cm^{-1} when $100Fe_{10}Mo$ was pretreated in H_2 at 280 °C, which moved towards high wavenumber direction (1836 and 1829 cm^{-1}) when pretreated in H_2 at 350 °C (Fig. 3A, B and D). Similarly, in comparison with CO pretreatment, a blue shift was observed for the catalyst pretreated in H_2 (Fig. 3B–D). According to Blyholder's model,[50] the blue shift can be interpreted as a decrease in the backbonding from the iron d orbital into the CO 2π orbital. Namely, the activation of carbon–oxygen bond in CO becomes less efficient with the blue shift in wavenumber. This result indicated that the strong interaction of Fe and Mo disfavored the activation of CO on the Fe active sites, which primarily accounts for the loss in the intrinsic activity of active Fe sites at high Mo loading levels.

4. Conclusion

For the FeMo catalysts, a migration of MoO_x from the bulk of the FeMo catalyst followed by dispersion along the catalyst surface into mono- and polymolybdates occurred during pretreatment in H_2. The Mo coverage was promoted by the rise of pretreatment temperature and the Mo amount in the catalyst. The Mo coverage facilitated the formation of small iron particles and stabilized these nano iron particles during the FTS reaction. Meanwhile it disfavored the reduction of hematite into α-Fe during the activation step and caused a strong Fe–Mo interaction particularly at high Mo amount. The strong Fe–Mo interaction weakened the activation of CO molecule on active Fe sites, which primarily accounts for the decline in the intrinsic activity (TOF_{CO}) of active Fe sites.

Conflicts of interest

There are no conflicts to declare.

Acknowledgements

We thank the National Outstanding Young Scientists Foundation of China (20625620) and the National Natural Science Foundation of China (20703054 and 20590361). This work is also supported by Synfuels China Co., Ltd.

References

1 G. P. Van Der Laan and A. Beenackers, *Catal. Rev.: Sci. Eng.*, 1999, **41**, 255–318.
2 H. Schulz, *Appl. Catal., A*, 1999, **186**, 3–12.
3 H. Jahangiri, J. Bennett, P. Mahjoubi, K. Wilson and S. Gu, *RSC Adv.*, 2015, **5**, 2210–2229.
4 O. O. James, B. Chowdhury, M. A. Mesubi and S. Maity, *RSC Adv.*, 2012, **2**, 7347–7366.
5 Y. Zhang, M. Ding, L. Ma, T. Wang and X. Li, *RSC Adv.*, 2015, **5**, 58727–58733.
6 Y. Zhang, L. Ma, T. Wang and X. Li, *RSC Adv.*, 2015, **5**, 45426–45430.
7 Y. Yang, H. W. Xiang, Y. Y. Xu, L. Bai and Y. W. Li, *Appl. Catal., A*, 2004, **266**, 181–194.
8 C. H. Zhang, Y. Yang, B. T. Teng, T. Z. Li, H. Y. Zheng, H. W. Xiang and Y. W. Li, *J. Catal.*, 2006, **237**, 405–415.
9 Y. Liu, J.-F. Chen and Y. Zhang, *RSC Adv.*, 2015, **5**, 29002–29007.
10 J. Wu, L. Qin, C. Wang, B. Lv, L. Wang, J. Chen and Y. Xu, *RSC Adv.*, 2016, **6**, 38356–38364.
11 M. Qing, Y. Yang, B. S. Wu, J. Xu, C. H. Zhang, P. Gao and Y. W. Li, *J. Catal.*, 2011, **279**, 111–122.
12 H. M. T. Galvis, A. C. J. Koeken, J. H. Bitter, T. Davidian, M. Ruitenbeek, A. Iulian Dugulan and K. P. de Jong, *J. Catal.*, 2013, **303**, 22–30.
13 C. F. Huo, B. S. Wu, P. Gao, Y. Yang, Y. W. Li and H. Jiao, *Angew. Chem., Int. Ed.*, 2011, **50**, 7403–7406.
14 X. Chen, D. Deng, X. Pan, Y. Hu and X. Bao, *Chem. Commun.*, 2015, **51**, 217–220.
15 M. D. Shroff, D. S. Kalakkad, K. E. Coulter, S. D. Kohler, M. S. Harrington, N. B. Jackson, A. G. Sault and A. K. Datye, *J. Catal.*, 1995, **156**, 185–207.
16 E. de Smita and B. M. Weckhuysen, *Chem. Soc. Rev.*, 2008, **37**, 2758–2781.
17 G. S. Ranhotra, A. T. Bell and J. A. Reimer, *J. Catal.*, 1987, **108**, 40–49.
18 S. T. Liu, A. C. Gujar, P. Thomas, H. Toghiani and M. G. White, *Appl. Catal., A*, 2009, **357**, 18–25.
19 W. P. Ma, E. L. Kugler, J. Wright and D. B. Dadyburjor, *Energy Fuels*, 2006, **20**, 2299–2307.
20 W. P. Ma, E. L. Kugler and D. B. Dadyburjor, *Stud. Surf. Sci. Catal.*, 2007, **163**, 125–140.
21 N. Lohitharn, J. G. Goodwin Jr and E. Lotero, *J. Catal.*, 2008, **255**, 104–113.
22 S. D. Qin, C. H. Zhang, J. Xu, B. S. Wu, H. W. Xiang and Y. W. Li, *J. Mol. Catal. A: Chem.*, 2009, **304**, 128–134.
23 R. M. M. Abbaslou, J. Soltan and A. K. Dalai, *Fuel*, 2011, **90**, 1139–1144.
24 S. D. Qin, C. H. Zhang, J. Xu, Y. Yang, H. W. Xiang and Y. W. Li, *Appl. Catal., A*, 2011, **392**, 118–126.
25 X. Cui, J. Xu, C. H. Zhang, Y. Yang, P. Gao, B. Wu and Y. W. Li, *J. Catal.*, 2011, **282**, 35–46.
26 W. P. Ma, E. L. Kugler and D. B. Dadyburjor, *Energy Fuels*, 2010, **24**, 4099–4110.
27 J. Y. Shen, T. Matsuzaki, T. Hanaoka, K. Takeuchi and Y. Sugi, *Catal. Lett.*, 1994, **28**, 329–336.
28 E. Guglielminotti, E. Giamello, F. Pinna, G. Strukul, S. Martinengo and L. Zanderighi, *J. Catal.*, 1994, **146**, 422–436.

29 P. Reyes, J. Fernández, I. Concha and G. Pecchi, *Catal. Lett.*, 1995, **34**, 331–341.
30 J. Y. Park, Y. J. Lee, P. K. Khanna, K. W. Jun, J. W. Bae and Y. H. Kim, *J. Mol. Catal. A: Chem.*, 2010, **323**, 84–90.
31 O. F. Oyerinde, C. L. Weeks, A. D. Anbar and T. G. Spiro, *Inorg. Chim. Acta*, 2008, **361**, 1000–1007.
32 D. L. A. de Faria, S. V. Silva and M. T. de Oliveira, *J. Raman Spectrosc.*, 1997, **28**, 873–878.
33 C. G. Hill Jr and J. H. Wilson III, *J. Mol. Catal.*, 1990, **63**, 65–94.
34 G. Mestl and T. K. K. Srinivasan, *Catal. Rev.: Sci. Eng.*, 1998, **40**, 451–570.
35 C. Li, *J. Catal.*, 2003, **216**, 203–212.
36 H. J. Tian, C. A. Roberts and I. E. Wachs, *J. Phys. Chem. C*, 2010, **114**, 14110–14120.
37 K. V. R. Chary, K. R. Reddy, G. Kishan, J. W. Niemantsverdriet and G. Mestl, *J. Catal.*, 2004, **226**, 283–291.
38 A. Christodoulakis, E. Heracleous, A. A. Lemonidou and S. Boghosian, *J. Catal.*, 2006, **242**, 16–25.
39 Z. Li, Y. Fu, M. Jiang, T. Hu, T. Liu and Y. Xie, *J. Catal.*, 2001, **199**, 155–161.
40 D. S. Kim, K. Segawa, T. Soeya and I. E. Wachs, *J. Catal.*, 1992, **136**, 539–553.
41 J. Leyrer, *Surf. Sci.*, 1988, **201**, 603–623.
42 H. G. Wendlandt and O. Glemser, *Angew. Chem.*, 1963, **75**, 949–957.
43 O. Glemser and R. V. Haeseler, *Z. Anorg. Allg. Chem.*, 1962, **316**, 168–181.
44 J. Leyrer, M. I. Zaki and H. Knözinger, *J. Phys. Chem.*, 1986, **90**, 4775–4780.
45 K. V. R. Chary, K. R. Reddy, G. Kishan, J. W. Niemantsverdriet and G. Mestl, *J. Catal.*, 2004, **226**, 283–291.
46 A. Christodoulakis, E. Heracleous, A. A. Lemonidou and S. Boghosian, *J. Catal.*, 2006, **242**, 16–25.
47 J. Wang, W. Li, C. Yu, Y. Chen and Y. Zhang, *React. Kinet. Catal. Lett.*, 1997, **62**, 217–224.
48 M. Jiang, N. Koizumi and M. Yamada, *J. Phys. Chem. B*, 2000, **104**, 7636–7643.
49 E. Boellaard, A. M. van de Kraan and J. W. Geus, *Appl. Catal., A*, 1996, **147**, 207–227.
50 G. Blyholder, *J. Phys. Chem.*, 1964, **68**, 2772–2777.